HHS Public Access

Author manuscript

Cancer Res. Author manuscript; available in PMC 2021 August 01.

Published in final edited form as:

Cancer Res. 2021 February 01; 81(3): 567–579. doi:10.1158/0008-5472.CAN-20-1865.

Altered mitochondria functionality defines a metastatic cell state in lung cancer and creates an exploitable vulnerability

Chen-Hua Chuang[1,#], **Madeleine Dorsch**[2,#], **Philip Dujardin**[2,#], **Sukrit Silas**[3], **Kristina Ueffing**[2], **Johanna M. Hölken**[2], **Dian Yang**[4], **Monte M. Winslow**[1,4,5,6], **Barbara M. Grüner**[2,7,*]

[1]Department of Genetics, Stanford University School of Medicine, Stanford, CA, USA

[2]Department of Medical Oncology, West German Cancer Center, University Hospital Essen at the University Duisburg-Essen, Germany

[3]Department of Chemical and Systems Biology, Stanford University School of Medicine, Stanford, CA, USA

[4]Cancer Biology Program, Stanford University School of Medicine, Stanford, CA, USA

[5]Department of Pathology, Stanford University School of Medicine, Stanford, CA, USA

[6]Stanford Cancer Institute, Stanford University School of Medicine, Stanford, CA, USA

[7]German Cancer Consortium (DKTK) partner site Essen, Germany

Abstract

Lung cancer is a prevalent and lethal cancer type that leads to more deaths than the next four major cancer types combined. Metastatic cancer spread is responsible for most cancer deaths but the cellular changes that enable cancer cells to leave the primary tumor and establish inoperable and lethal metastases remain poorly understood. To uncover genes that are specifically required to sustain metastasis survival or growth, we performed a genome-scale pooled lentiviral-shRNA library screen in cells that represent non-metastatic and metastatic states of lung adenocarcinoma. Mitochondrial ribosome and mitochondria-associated genes were identified as top gene sets associated with metastasis-specific lethality. Metastasis-derived cell lines *in vitro* and metastases analyzed *ex vivo* from an autochthonous lung cancer mouse model had lower mitochondrial membrane potential and reduced mitochondrial functionality than non-metastatic primary tumors. Electron microscopy of metastases uncovered irregular mitochondria with bridging and loss of normal membrane structure. Consistent with these findings, compounds that inhibit mitochondrial translation or replication had a greater effect on the growth of metastasis-derived cells. Finally, mice with established tumors developed fewer metastases upon treatment with phenformin *in vivo*. These results suggest that the metastatic cell state in lung adenocarcinoma is associated with a specifically altered mitochondrial functionality that can be therapeutically exploited.

[*]**Corresponding author contact information:** Barbara Maria Grüner, Department of Medical Oncology, West German Cancer Center, University Hospital Essen at the University Duisburg-Essen, Hufelandstr. 55, 45147 Essen, Germany, phone: +49 201 723 8142; fax: +49 201 723 6825; Barbara.gruener@uk-essen.de.

[#]Equal contribution

Competing interests: The authors declare no competing interests.

INTRODUCTION

Lung cancer is the most lethal cancer type, causing over 145,000 deaths per year in the United States alone (1). Metastatic cancer spread is a major reason for cancer-related deaths. However, despite the importance of targeted therapies directed against advanced stage cancer, treatment options for metastatic cancer remain limited. Genomic analysis of human lung adenocarcinoma, which is a major lung cancer sub-type, has led to the identification of targetable oncogenic alterations including EGFR mutations and ALK translocations (2–7). Despite the clinical value of targeted therapies directed towards these cancer-specific alterations, many tumors do not contain genomic alterations that can be targeted for therapeutic benefit. Furthermore, even when targeted therapies exist, responses are often short lived. Hence there remains a critical need to better understand the metastatic cancer state and uncover targetable pathways that are specific to late-stage cancer.

Global gene expression analysis of human tumors has uncovered changes in gene expression programs that predict patient outcome. These studies have contributed to our understanding of the mechanisms that lead to cancer progression and drug resistance (8). Unfortunately, these studies have only rarely identified key therapeutic targets as gene expression does not necessarily implicate function. Alternatively, functional genomics focuses on unbiased screening coupled with functional readouts to uncover pathways that could have therapeutic potential (9). Extensive efforts to quantify the effect of pooled shRNA and sgRNA libraries across panels of human cell lines have revealed important mediators of cancer cell survival (10, 11). However, the relatively small number of cell lines from individual cancer types, extensive genomic heterogeneity, and derivation from primary tumors and metastases of different origins often render these studies underpowered to identify molecular features that uniquely distinguish the non-metastatic from the metastatic cell state. These complications suggest that more defined models may have increased sensitivity and specificity to uncover novel aspects of valuable therapeutic targets.

To better understand the biological forces that drive lung cancer progression, genetically engineered mouse models of human lung adenocarcinoma have been generated with conditional alleles to express oncogenic Kras and inactivate the p53 tumor suppressor (12–14). Notably, this $Kras^{G12D;Trp53^{KO}}$ lung adenocarcinoma model recapitulates the genetic events and histological appearance of early and late stage human tumors (3, 15). Thus, this model system represents a useful *in vivo* and *ex vivo* tool to identify novel regulators of lung adenocarcinoma progression and metastasis (16).

We previously generated cell lines from non-metastatic primary lung tumors (T_{nonMet}) and metastases (Met) from the $Kras^{G12D;Trp53^{KO}}$ mouse model (14, 16). These T_{nonMet} and Met cell lines maintain their differences in metastatic ability, exhibit dramatic differences in gene expression programs, and analysis of these cell lines has contributed to the discovery of several regulators of the metastatic process (14, 17–19). Expression of individual regulators and the overall gene expression program can predict human lung adenocarcinoma patient outcome, suggesting that these cell lines recapitulate at least some aspects of the metastatic state of human lung tumors (14, 17–19). This unique set of cell lines from early stage non-

metastatic tumors and late-stage metastases provides an opportunity to investigate whether cancer progression creates unique vulnerabilities that can be exploited therapeutically.

To systematically uncover genes that are specifically required to sustain the growth and/or survival of cancer cells in the metastatic cell state, we performed a pooled genome-scale lentiviral-shRNA library screen. A targeted secondary *in vivo* screen validated top candidates, including a highly significant enrichment for mitochondria and mitochondria ribosome gene-sets associated with metastasis specific lethality. Analyses of mitochondrial membrane potential, reactive oxygen species (ROS) levels, mitochondrial respiration, glycolytic, and fuel utilization assays, as well as electron microscopy confirmed dysfunctionality of mitochondria as a discriminating feature of the metastatic state. These observations highlight a metastasis-specific vulnerability that can be therapeutically exploited with pharmacological targeting to block metastasis *in vivo*.

MATERIALS AND METHODS

Selected methods are detailed in this section. An extensive version of this section is available as Supplementary Methods within the Supplementary Material of this manuscript.

Mice

$Kras^{LSL\text{-}G12D}$, $Trp53^{flox}$ and $Rosa26^{LSL\text{-}tdTomato}$ mice have been described previously (12, 16). Tumors were initiated by intratracheal infection of mice with lentiviral vectors expressing Cre-recombinase as previously described (20). All animal studies and procedures were performed according to and approved by the Stanford Institute of Medicine Animal Care and Use Committee. Animals of both sexes were used.

Cell lines

The 368T1 and 394T4 cell lines were generated from primary lung tumors, the 238N1 and 482N1 cell lines were generated from lymph node metastases, the 404M1, 2691M1 cell lines were generated from distant organ metastasis, the 889PF from disseminated cancer cells within the pleural cavity, and the 579DLN cell line was generated from a distant lymph node metastasis of lung-adenocarcinoma-bearing $Kras^{LSL\text{-}G12D/+};Trp53^{flox/flox}$ ($Kras^{G12D};Trp53^{KO}$) $Kras^{LSL\text{-}G12D/+};Trp53^{flox/flox};Rosa26^{LSL\text{-}Tomato/+}$ ($Kras^{G12D};Trp53^{KO};R26^{Tomato}$) mice (14, 16). All cell lines were regularly (~ monthly) confirmed to be mycoplasma negative. 293T cell lines were obtained from ATCC (ATCC Cat# CRL-3216, RRID:CVCL_0063) and identity was regularly confirmed by STR analysis. All cell lines were passaged at least once after thawing before use in subsequent experiments. The average time in culture was 4 weeks (range between 2 and 6 weeks), then a new vial was thawed.

Cell line RNA-sequencing library preparation and analysis

Total RNA was isolated from 1×10^6 cells of each line (368T1, 394T4, 238N1, and 482N1) using the Qiagen RNeasy mini kit. For each sample, 1 μg of total RNA was used for library construction. The integrity and quality of RNA was assessed prior to library construction using an Agilent Bioanalyzer. RNA-sequencing libraries were prepared using the Illumina

TruSeq RNA kit according to manufacturer's instructions. High-throughput sequencing was performed on Illumina HiSeq. For analysis of the RNA-seq reads, we performed differential gene and transcript expression analysis using TopHat (TopHat, RRID:SCR_013035) and Cufflinks (Cufflinks, RRID:SCR_014597). RNA-seq reads were separately aligned to the mouse genome (mm9) and the aligned RNA-seq reads were assembled into transcripts. Annotated transcripts were obtained from the UCSC genome browser (http://genome.ucsc.edu, UCSC Genome Browser, RRID:SCR_005780) and the Ensembl database (Ensembl, RRID:SCR_002344). Transcript abundances were measured in Fragments Per Kilobase of exon per Million fragments mapped (FPKM). Finally, Cuffdiff (Cuffdiff, RRID:SCR_001647) was used to define differential expression. The data have been deposited in NCBI's Gene Expression Omnibus ((GEO), RRID:SCR_005012) and are accessible through GEO Series accession number GSE159169 (https://www.ncbi.nlm.nih.gov/geo/query/acc.cgi?acc=GSE159169).

Genome-wide shRNA screen

Lentiviral particles from the 100K mouse shRNA pool (obtained from Broad Institute: The RNAi Consortium (21)) were transduced at low MOI (0.3; each shRNA was stably integrated into an average of 600 cells) into 4 cell lines (368T1, 394T4, 238N1 and 482N1; 3 replicates per cell line). Virus transduction and cell line passaging were performed according to the method described by Chueng et al. (22) with minor modification. In brief, the virus and cell mixture was seeded into a 12-well plate at ~2 mL per well, and cells were transduced by spinoculation at 1000 g for 2 hours with 12 μg/ml polybrene at 30 °C. After 24 hours, the 12 wells from each replicate transduction were pooled, and the combined cells were transferred into a 15-cm dish. Cells were selected with 4 μg/ml puromycin starting day 4 post-transduction. For all subsequent passages, 7.2×10^7 cells per replicate were carried over. The remaining cells for all passages were collected, resuspended in 1 mL of PBS, and stored at −20 °C for genomic DNA isolation. Passaging for each cell line was continued for at least 22 population doublings. Puromycin selection was maintained for the entire experiment.

To identify the shRNA sequences enriched in screened cells, genomic DNA was isolated from cells collected at each timepoint, and hairpin sequences were quantified using Illumina DNA sequencing (23).

Statistical analysis of the screen

We applied the RNAi Gene Enrichment Ranking (RIGER), Kolmogorov-Smirnov (KS), and Weighted Sum (WS) algorithms to evaluate candidate genes from the pooled shRNA screens. Kolmogorov-Smirnov (KS) is nonparametric and calculates gene scores from a collection of shRNA phenotype profiles, similar to the method described by Luo et al. (24). Weighted Sum (WS) algorithms takes the combined sum of the first and second best ranks for hairpins for each gene. The best ranking hairpin is given a weight of 0.25 and the second best ranking hairpin is given a weight of 0.75. The weighted values (WS score) are determined by the sum of the first and the second weighted ranks, and genes are ranked by this WS score (https://software.broadinstitute.org/GENE-E/extensions.html). We considered all three ranking approaches to generate a list of top 50 candidate genes (Supplemental Fig.

S2A) whose knock-down was found to impact only the Met cell lines in the screen (238N1 and 482N1), or only the Non-Met cell lines (368T1 and 394T4), or each cell line individually. Heatmaps for each set of genes were generated using the heatmap.2 function from the R package gplots (V 3.0.3). Clustering (depicted in Figures 1C and D) was performed according to https://software.broadinstitute.org/GENE-E/doc.html. Each box represents the measure of global correlation between the entire dataset for one cell line versus another.

Secondary screen

A list of candidate genes was generated from the initial screen as described above. Additionally, control genes (12 “lethal to all” and 5 “advantageous to all”, as well as 32 inert genes) were chosen (Supplemental Fig. S2A). For the secondary validation screen, a pooled library of 512 TRC shRNA clones was produced by cherry picking these clones from the sequence-validated TRC shRNA library used in the first screen. Each gene was targeted by 2 shRNAs.

The viral packaging and collection procedure was established based on the manufacturer’s guidelines (https://portals.broadinstitute.org/gpp/public/resources/protocols). In brief, 293T cells were plated in ten 15cm dishes (Falcon/Corning, Tewksbury, MA, USA) at 80.000 cells per cm^2 in DMEM (Gibco, Grand Island, NY, USA, Carlsbad, CA, USA) supplemented with 10% FCS (Invitrogen), 2 mM L-Glutamine (Invitrogen) and Penicillin-Streptomycin (Invitrogen). The next day, for each plate separately, a Packaging-Plus Mix was prepared consisting of 6 μg of shRNA library, 10 μg psMD2.G, 20 μg psPAX2 and 60 μL PLUS Reagent (Invitrogen) in a total volume of 1.3 ml OptiMEM (Invitrogen) and incubated for 15 minutes. In order to obtain a transfection mix, 1.4 ml of OptiMEM containing 90 μL of Lipofectamine (Invitrogen) was added to the Packaging-Plus Mix and incubated for another 15 minutes before adding dropwise to the plated 293T cells. The medium was changed 24 hours post-transfection. The medium from both the 48 hours and the 72 hours harvests after transfection was combined and filtered through a 0.45 μm PES filter (Nalge Nunc, Rochester, NY, USA). Lentivirus aliquots were stored at −80 °C until used for transduction of the selected cell lines.

To perform large-scale infections, 3.6×10^6 target cells (MOI 0.3; each shRNA was stably integrated into an average of 2000 cells) were transduced for each replicate. The virus-cell mixture was split across a 12-well plate at 2 ml per well. A spin infection was performed by centrifugation at 1000 g for 2 h at 30 °C. After 20 h, the 12 wells from each replicate infection were pooled, and the combined cells were transferred into a 15 cm dishes. Transduced cells were selected with 4 μg/ml puromycin from day 4 after infection. For all subsequent passages, 1.2×10^6 cells per replicate were carried over. The remaining cells for all passages were collected, resuspended in 1 mL of PBS, and stored at −20 °C for genomic DNA isolation. Passaging for each cell line was continued for at least 22 population doublings. Puromycin selection was maintained for the entire experiment.

To validate genes that were specifically required for the survival or growth *in vivo*, 3×10^6 puromycin-selected transduced cells (238N1, 482N1) were injected into back flanks of 3 NSG recipient mice. Mice were analyzed 4 weeks after transplantation. Tumors were

disaggregated to single-cell suspensions by mincing with razor blades and treated with collagenase IV, dispase, and trypsin at 37°C for 30 minutes. Genomic DNA was isolated from cells collected from each tumor, and hairpin sequences were quantified using Illumina DNA sequencing as described above.

Statistical analysis of secondary screen

To normalize the read count of each hairpin, raw read counts were divided by total counts of each sample (per million). Hairpins with normalized count values < 10 for across all early time point samples were eliminated from downstream analyses. Changes in shRNA representation over time were calculated by average read counts of late time points minus early time points.

GO Term and Gene Set Enrichment Analysis (GSEA)

To discover pathways driving pan- or metastasis-specific lethality top candidate genes identified in the screen were mapped to their direct human ortholog using information provided in the Mouse Genome Database (25) at www.informatics.jax.org. For GSEA analysis (26) (SeqGSEA, RRID:SCR_005724), a rank-ordered list of candidate genes was analyzed using GSEA v2.2.0 software available from the Broad Institute (http://www.broad.mit.edu/gsea) and GO term analysis from The Database for Annotation, Visualization and Integrated Discovery (DAVID) (https://david.ncifcrf.gov/, DAVID, RRID:SCR_001881). Only genes with a human homolog were used for this analysis.

Tumor dissociation and cell sorting

For cell sorting, primary tumors and metastases were dissociated using collagenase IV, dispase, and trypsin at 37 °C for 30 minutes. After dissociation, the samples were continually on ice, in contact with ice-cold solutions, and in the presence of 2 mM EDTA and 1 U/ml DNase to prevent aggregation. Cells were stained with antibodies to CD45 (BioLegend Cat# 103133, RRID:AB_10899570), CD31 (BioLegend Cat# 102423, RRID:AB_2562186), F4/80 (BioLegend Cat# 123131, RRID:AB_10901171), and Ter119 (BioLegend Cat# 116233, RRID:AB_10933426) to exclude hematopoietic and endothelial cells (defined in combination as $\text{Lineage}^{\text{negative}}$). To analyze mitochondria membrane potential, cells were stained with 200 nM Mitotracker deep red (Invitrogen) for 15 min at 37 °C. A fixed number of GFP-positive control cells was spiked into each sample for normalization to account for staining artifacts due to different cell numbers in the samples. DAPI was used to exclude dead cells. FACSAria™ sorters (BD Biosciences) were used for analysis. To analyze ATP levels, equal numbers of cells were analyzed with the reversed CellTiter-Glo Luminescent Cell Viability Assay (Promega) according to manufacturer's instructions, using an ATP standard curve for calibration.

Cell line transplantation and analysis

6- to 10-week-old NSG mice of similar weights, randomized for both male and female animals, were used for cell transplantation experiments. For the subcutaneous injections, 5×10^4 889PF or 579DLN cells were injected into both flanks of NSG recipient mice. Treatment of mice was started 7 days after transplantation with either 100 mg/kg phenformin

or vehicle by oral gavage or 9 days after transplantation with either 1mg/kg doxycycline or vehicle by intraperitoneal injection once daily. Mice were analyzed 3 or 4 weeks after transplantation, respectively. For the intravenous injections 579DLN cells were treated with either phenformin [200 μM] or vehicle for 48 hours *in vitro*. Then cells were trypsinized and 1×10^5 cells were injected intravenously into the lateral tail vein. Starting at the day of injection, mice were treated daily either with 100 mg/kg phenformin or with vehicle control by oral gavage. For the short-term intravenous experiment, 579DLN cells were treated with either phenformin [200 μM], doxycycline [15 μg/ml], FCCP [2 μM], or vehicle for 48 hours *in vitro*. Then cells were trypsinized and 5×10^5 cells were injected intravenously into the lateral tail vein of immunocompetent 129/Bl6 F1 mice. Mice were sacrificed either three or seven days after injection and lungs were harvested, weighed, and analyzed by fluorescence microscopy and flow cytometry. During analysis of the animals the performing scientist was blinded towards experimental groups. No statistical method was used to predetermine sample size. The Stanford Institute of Medicine Animal Care and Use Committee or the Landesamt für Natur, Umwelt- und Verbraucherschutz des Landes Nordrhein-Westfalen (LANUV) approved all animal studies and procedures, respectively.

Statistics

Graphs and statistics were generated using the GraphPad Prism software (GraphPad Prism, RRID:SCR_002798). Significance, where indicated, was calculated using the Wilcoxon test for non-normally distributed data. Significance was determined as a p-value < 0.05. No statistical method was used to predetermine sample size.

RESULTS

To systematically uncover genes that are specifically required for survival or growth of metastatic cancer cells, we performed a pooled lentiviral-shRNA library screen in two T_{nonMet} (368T1 and 394T4) and two Met (238N1 and 482N1, both from lymph node metastases) lung cancer cell lines derived from the $Kras^{G12D};Trp53^{KO}$ mouse model (Fig. 1A,B). This screen included > 92,000 shRNAs targeting ~20,000 genes thus enabling a broad interrogation of cancer cell states and having the potential to uncover genes essential for growth of metastatic cells. Importantly, both T_{nonMet} and Met lines share similar oncogenic and tumor suppressor alterations which likely increases our ability to detect significant effects and implicate candidate genetic targets. To identify genes that are essential for each cell line, we used high-throughput sequencing of the shRNAs in the cancer cell populations before and after 22 population doublings (“Early time point” and “Late time point”, respectively, Fig. 1A). As anticipated, many shRNA targets were lethal to all cell lines, which led to clustering of the “Early time point” samples away from the “Late time point” samples (Fig. 1C, Supplementary Data Table S1). Among “Late time point” samples, the diversity between Met cell lines was greater when compared to each other than the diversity among T_{nonMet} cell lines (Fig. 1D). shRNAs that were underrepresented in all cell lines were greatly enriched for genes with known essential pathway functionality (Fig. S1A–D). Importantly, this genome-scale screen identified genes specifically required for the survival or growth of cancer cells in either the non-metastatic state or the metastatic state as

well as for individual cell lines (Fig. 1E, Supplementary Fig. S1E, Supplementary Data Table S2).

Comparative analyses using Kolmogorov-Smirnov (KS), Weighted Sum (WS), and best-ranking shRNA algorithms revealed a list of shRNAs and genes most prominently differentially affecting the growth of T_{nonMet} versus Met cell lines (Supplementary Data Tables S3–S5). To investigate the expression of these genes in the T_{nonMet} (368T1 and 394T4) and the Met (238N1 and 482N1) cell lines, we also performed RNA-sequencing based gene expression analysis (Supplementary Data Table S6). We incorporated pathway-level analysis based on identified shRNA effect and expression levels to define candidates for further functional validation. Based on these analyses, we performed a secondary screen using 2 of the initially used shRNAs targeting each of 240 top metastasis-specific lethal candidate genes in two T_{nonMet} cell lines (368T1 and 394T4) and four metastasis derived cell lines (238N1 and 482N1 from lymph node metastases, as well as 404M1 and 2691M1 from distant metastases). This secondary screen included positive control shRNAs that were lethal to all cell lines, control shRNAs (inert) that should have no effect, and shRNAs that were found to provide a competitive growth advantage to all cell lines (Supplementary Fig. S2A). This focused secondary screen was performed in the same manner as the initial screen and generated a robust readout of the effect of candidate gene knockdown, with high reproducibility among replicates (Supplementary Fig. S2B). All the control shRNAs performed as anticipated: lethal shRNAs had reduced representation in all cell lines, advantageous shRNAs gained representation in all cell lines, and inert shRNAs had no effect. Importantly, many of the candidate metastasis-specific lethal shRNAs had reduced representation specifically in metastasis-derived cancer cells, validating our findings from the initial screen (Fig. 2B–E, Supplementary Fig. S2C, D, and Supplementary Data Table S7). Furthermore, in parallel with this *in vitro* screen, we also transplanted two of the Met cell lines (238N1 and 482N1) transduced with the lenti-shRNA validation pool subcutaneously into mice to assess the effect of each shRNA on growth *in vivo* (Supplementary Data Table S8). The data obtained from this *in vivo* screen were consistent with the results obtained *in vitro*, further validating our screening results (Fig. 2F, G).

Our primary and secondary shRNA screens, including data from both *in vitro* and *in vivo* experiments, uncovered several top candidate genes whose shRNA-mediated suppression was specifically detrimental to cancer cells in a metastatic state (Fig. 3A and B, Supplementary Fig. S3A and Supplementary Data Table S9). To prioritize hits and investigate cellular programs specifically required for the growth of Met cells, we performed gene set enrichment and GO-term analyses of our initial screening data. Interestingly, both analyses revealed mitochondria (mt), the mitochondria ribosome and mitochondria ribosomal subunit gene sets as the top gene sets that, when targeted, were specifically lethal to Met cells (Fig. 3C). Indeed, RNA-Sequencing of T_{nonMet} and Met cell lines revealed that mitochondria-encoded genes were more highly expressed in Met cells whereas most of the nuclear-encoded mitochondrial ribosome proteins were more highly expressed in T_{nonMet} cells (Supplementary Fig. S3B).

We initially tested whether this distinct response to mt-targeting shRNAs might be attributable to mitonuclear imbalance. Mitonuclear imbalance is the stoichiometric

imbalance between nuclear genome and mt genome-encoded oxidative phosphorylation proteins (27). Interestingly, RNA-Seq on primary tumors and metastases isolated from the *Kras*^{G12D};*Trp53*^{KO} mouse model (16) did not uncover significant differences in the overall expression of mt-encoded genes (Supplementary Fig. S3C), and western blot analysis of T_{nonMet} and Met cells for nuclear (Atp5a, Uqcrc2, Sdhb) and mt-encoded (mt-Co1) proteins of the respiratory chain complex did not identify differences in expression levels or patterns (Supplementary Fig. S3D). Thus, mitonuclear imbalance is unlikely to have driven the distinct response in our shRNA screen.

To further interrogate whether the metastatic cell state is characterized by altered mitochondrial functionality, we generated fluorescently labeled T_{nonMet} and Met cells and performed *in vitro* competition assays. Treatment with ethidium bromide (which impairs mitochondria DNA replication and transcription (28–30)), high concentrations of doxycycline (which inhibits mitochondrial translation (31, 32)), phenformin (a complex I inhibitor of the respiratory chain which causes lactic acidosis, a hallmark of mitochondrial impairment (33, 34)), or FCCP (carbonylcyanide p-trifluoromethoxyphenylhydrazone, a protonophore which dissociates electron transport from ATP synthesis and allows transport to proceed without synthesis (35)) were each consistently more detrimental to Met cells compared to T_{nonMet} cells, as the Met/^{TnonMet} ratio was decreasing in each treatment. Furthermore, also under more physiological low oxygen conditions (1% oxygen) all treatments affected Met cells more than T_{nonMet} cells, though to a lesser extent (Fig. 4A–D and Supplementary Fig. S4A–D). Thus, these pharmacological data were consistent with differences in mitochondrial functionality between primary tumor-derived and metastasis-derived lung cancer cells and suggest that mitochondria are a critical and pharmacologically targetable Met cell-specific vulnerability.

To determine whether the differential sensitivity to mitochondria-targeted therapy is indeed due to differences in mitochondria functionality, we performed Seahorse assays for oxygen consumption rate and mitochondrial function. Met cells (n = 3 cell lines per group) had reduced spare respiratory capacity and coupling efficiency compared to T_{nonMet} cells (Fig. 4E–G). Furthermore, higher ECAR/OCR (extracellular acidification rate/oxygen consumption rate) ratio and higher ECAR levels pointed to a higher use of glycolysis as primary metabolic pathway in Met cells (Fig. 4H, Supplementary Fig. S4E). In addition, Seahorse assays for fuel dependency revealed that, while fatty acids do not appear to play a significant role as a fuel source in either T_{nonMet} or Met cells, Met cells showed a higher dependency on glycolysis-derived pyruvate and were less able to utilize glutamine (Fig. 4I–L, Supplementary Fig. S4F and S4G). Analysis of relative ATP levels produced in galactose containing media revealed no significant difference in the capacity to perform oxydative phosphorylation between Met and T_{nonMet} cells (Fig. 4M) and the ratio of ATP production in glucose versus galactose containing media was also not significantly different (Fig. 4N). However, comparing relative growth rates of cells growing in glucose or galactose containing media revealed that T_{nonMet} cell were less affected when solely being able to perform oxydative phosphorylation instead of glycolysis compared to Met cells (Fig. 4O). Taken together, these results suggest that metastatic lung cancer cells have a reduced usage rate of glutamine as fuel during oxidative phosphorylation, reduced fuel flexibility and might primarily utilize glycolysis to produce ATP but are not completely dependent on it.

Furthermore, we performed flow cytometry to assess mitochondria membrane potential in T_{nonMet} and Met cell lines using the JC1 dye. Met cells *in vitro* had significantly more depolarized mitochondria indicating lower membrane potential and functionality (Fig. 4P). However, treatment with any of the three mt-targeting compounds (phenformin, ethidiumbromide, or doxycycline) did not reveal significant differences in the relative change of depolarization levels between T_{nonMet} and Met cells (Supplementary Fig. S4H and S4I). This observation was further validated by analysis of reactive oxygen species (ROS) production. Met cells had higher baseline ROS levels in steady-state culture, yet under treatment conditions the relative changes in ROS level between Met and T_{nonMet} cells did not differ (Fig. 4Q, Supplementary Fig. S4J and S4K). Similarly, neither treatment with doxycycline nor ethidium bromide revealed a differential effect on T_{nonMet} or Met cell mitonuclear imbalance (Supplementary Fig. S4L). Finally, no distinct effects of phenformin on major signalling pathways between Met and T_{nonMet} cells were detectable by western blot analysis (Supplementary Fig. S4M), and neither phenformin, nor doxycycline or ethidiumbromide significantly altered proliferation of either Met or T_{nonMet} cells (Supplementary Fig. S4N–Q). Interestingly, migratory capacity was generally higher in T_{nonMet} than Met cells, independent of normoxic, hypoxic (1% O_2) or acidic (pH 6.5) conditions (Supplementary Fig. S4R–U), and we confirmed that Met cells might be partially reprogrammed towards a more “stem-like” phenotype as they all could form and grow spheres in three-dimensional culture whereas only one out of three T_{nonMet} cells was able to grow (Supplementary Fig. S4V, W). Collectively, these results indicate that the net-effect of mt-targeting drugs is the same in both cancer states, but the steady-state of mt function is lower in Met cells, rendering them more susceptible to treatment.

To determine whether this altered mitochondrial functionality is also present *in vivo*, we initiated lung tumors in $Kras^{G12D};Trp53^{KO};R26^{Tomato}$ mice, sorted $Tomato^{positive}$ cancer cells from primary tumors and distant metastases, and measured the mitochondrial membrane potential using Mitotracker deep red. Cancer cells isolated from metastases had significantly more depolarized mitochondria than cancer cells from primary tumors, indicating a higher fraction of dysfunctional mitochondria (Fig. 5A), even though ATP-production was not significantly affected (Fig. 5B). Indeed, electron microscopy analysis of tissue sections from primary tumors and pleura metastases from $Kras^{G12D};Trp53^{KO};R26^{Tomato}$ mice revealed that while the total number of mitochondria is the same in primary tumors and metastases, the number of abnormal mitochondria (characterized by loss of density and bridging of cristae, indicating a disturbed respiratory chain setup) is significantly higher in metastasis cells (Fig. 5C–E). These results indicate that the altered mitochondria functionality discovered in Met cells *in vitro* is also present in metastatic cancer cells *in vivo*.

To further explore whether this change in mitochondria functionality of Met cells creates a specific and pharmacologically addressable vulnerability *in vivo*, we utilized a subcutaneous transplantation mouse model which recapitulates several aspects of the metastatic cascade (16). In this model, Met cells are grown as primary subcutaneous tumors and the cancer cells metastasize spontaneously to the lung and liver. We treated mice with established primary tumors (7 days after transplantation) with either vehicle or 100 mg/kg phenformin p.o. once daily for three weeks and then quantified primary tumor weight and size, lung weight, and

the number and size of Tomato^{positive} metastases in the lungs. While primary subcutaneous tumors were of similar size and weight in both the control and phenformin treated groups, the number of metastases in the lungs of phenformin treated animals (as assessed by both macroscopic fluorescent stereomicroscope and microscopic IHC analysis) was reduced by ~3-fold (Fig. 5F–H). Furthermore, we repeated this experimental setup and treated animals with established primary subcutaneous tumors (9 days after transplantation) with either vehicle or 1 mg/kg doxycycline i.p. once daily for three weeks. Here, primary subcutaneous tumors were slightly reduced in weight in doxycycline-treated animals, yet in 6 out of 8 mice the number of Tomato^{positive} cancer cells in the lungs was strongly decreased compared to control treated animals (Supplementary Fig. S5A–C). This indicates that mitochondria-targeting treatments reduce metastatic ability *in vivo* which is consistent with the Met-specific effect of mt-targeting compounds *in vitro*.

To further investigate the effect of phenformin on the later stages of the metastatic cascade *in vivo*, we intravenously injected mice with Met cells that were pre-treated with phenformin for 48 hours *in vitro* and subsequently continued dosing the mice with phenformin for 7 days. Tomato^{positive} cancer cells were reduced ~3-fold in the lungs of phenformin treated animals compared to control-treated mice ($p = 0.0002$). However, proliferation rates of cancer cells in the lungs did not differ between the groups (Fig. 5I–K). We then expanded the experimental setup into four groups: Met cells were either pre-treated with phenformin or vehicle *in vitro* and subsequently injected intravenously into recipient mice that received either further treatment with phenformin or vehicle for 3 days *in vivo*. Interestingly, pre-treatment of Met cells with phenformin before intravenous injection significantly reduced the number of Tomato^{positive} cancer cells in the lungs compared to controls, independent of whether the recipient mice were further treated with phenformin or vehicle (Supplementary Fig. S5D, E). This is consistent with a cancer cell autonomous effect of phenformin on metastatic ability, that was not due to induction of apoptosis or anoikis (Supplementary Fig. S5F, G). To further validate that other mitochondria-targeting compounds can impact metastatic ability, we intravenously injected Met cells pre-treated *in vitro* with either phenformin, doxycycline, FCCP or vehicle for 48 hours. After 3 days, lungs were harvested and analyzed by flow cytometry. Importantly, all three mitochondria-targeting agents reduced the number of Tomato^{positive} cancer cells in the lungs of recipient mice (Supplementary Fig. S5H, I). Taken together, mitochondrial function is significantly altered in metastatic cancer cells and this “Achilles heel” can be therapeutically exploited for benefit *in vivo*.

DISCUSSION

Loss-of function genetic screens have been widely applied as a powerful discovery tool in biology (36). We chose to take this approach using a high-throughput shRNA screen to functionally characterize the metastatic cell state and to potentially identify novel therapeutically exploitable targets that are specifically lethal to metastatic lung adenocarcinoma cells. For this we used T_{nonMet} and Met cell lines that were isolated from the well-established autochthonous *Kras^{G12D};Trp53^{KO}* mouse model of lung adenocarcinoma and are distinguished by their metastatic ability (14, 16–19). These cell lines have fewer confounding variables such as different origins and genetic diversity, thus

enabling us to identify genes that are differentially important for maintaining growth and/or viability of metastatic cells.

Here, we identify mitochondria as a cellular structure with a distinct functionality in non-metastatic primary tumor cells and metastatic cancer cells. We found that mitochondria in Met cells are functionally altered, both *in vitro* and *in vivo*. Mitochondria in Met cells have a disturbed morphology and lower membrane potential. *In vitro*, we found that this modified mitochondria functionality leads to reduced spare respiratory capacity and coupling efficiency, independent from specific cellular signaling. In addition, we found that treatment with mitochondria-targeting drugs results in Met and T_{nonMet} cells being affected at similar absolute levels, further strengthening our conclusion that mitochondria are structurally and functionally compromised in steady-state metastatic cancer cells and that upon further targeting are less able to compensate.

At first glance, it seems counterintuitive that the disruption of a vital cell organelle such as the mitochondria would lead to cells that are seemingly better adapted for metastasis. However, mitochondrial dysfunction has been observed in multiple types of cancer cells during the metastatic process (37). Mitochondria dysfunction can either describe changes in mitochondria metabolism or refer to changes in mitochondria dynamics. The former is a well-known and thoroughly studied topic (38), with the most prominent alteration being the Warburg effect, where dysfunctional mitochondria generate ATP by glycolysis even in the presence of oxygen (39). With the balance between glycolysis and oxidative phosphorylation disturbed, metabolite levels change and can promote hypoxia, enhancing further tumor progression (37, 38, 40). In addition, elevated levels of glycolysis increase the acidity of the tumor environment, further promoting invasion and metastasis by breaking down the extracellular matrix and driving apoptosis of normal cells (41, 42). On the other hand, recent efforts have focused on mitochondria structure and dynamics: alterations in mitochondrial proteostasis, bioenergetics, and trafficking is associated with extensive bioenergetic defects, including reduced oxygen consumption, decreased ATP generation, and aberrant production of reactive oxygen species (ROS) which have been suggested to promote tumor progression and metastasis by directly affecting tumor cell motility (43). Most recently, it was shown that mitochondrial dynamics are dysregulated in a variety of cancers, which in turn leads to specific and therapeutically exploitable sensitivities (44).

In our study, metastatic cancer cells show a higher dependency on glycolysis-derived pyruvate, primarily utilize glycolysis, and are less able to use glutamine, as indicated by a reduced rate of glutamine consumption as fuel during oxidative phosphorylation. Yet, while recent studies have shown that the monocarboxylate transporter-1 (MCT1) is responsible for providing lactate as a fuel of the TCA cycle in lung cancer (45) and both MCT1 and MCT2 have been found in melanoma and breast cancer to be important for their metastatic ability, respectively (46, 47), we did not identify either MCT1 or MCT2 as metastasis-specific hits in our screen. This could be either due to different metabolic functions in this tumor entity, due to an upregulation of these genes during the metastatic process when mitochondria become dysfunctional, or due to a metastasis-independent function of MCT1 and MCT2 so that their respective depletion is also lethal for non-metastatic tumor cells.

Classical anti-tumor approaches have largely focused on targeting DNA replication or DNA damage repair and the interruption of cell division to induce apoptosis (48). However, these processes are not cancer-specific and their therapeutic inhibition leads to severe side effects. Finding metastasis specific vulnerabilities, even if those vulnerabilities are related to conserved cellular functions, could allow for lower dosing and reduced patient side effects. Because of the importance of mitochondria during carcinogenesis and disease progression, researchers have started focusing on mitochondrial metabolism as a more selective target to induce cancer cell death. Utilizing this concept, multiple clinical studies have been, or are being, conducted mainly around the dual α-ketoglutarate dehydrogenase (KGDH) and pyruvate dehydrogenase (PDH) inhibitor CPI-613 and a compound called DCA, that inhibits pyruvate dehydrogenase kinase (PDK) and activates pyruvate dehydrogenase (PDH) (49). Yu and colleagues repurposed the FDA-approved arthritis drug leflunomide, which promotes mitochondrial elongation through its function as an agonist of the fusion GTPase MFN2 in pancreatic cancer (50).

We utilized phenformin as a proof-of-concept tool to specifically target Met cells *in vitro* and *in vivo*. Phenformin is an antidiabetic drug belonging to the class of biguanides. Due to its side effect of lactic acidosis it was withdrawn from the market in most countries in the 1970s. In contrast to metformin, phenformin has a lipophilic structure which allows a rapid entrance to the cell and mitochondria without transporters. Once assimilated in the mitochondria, phenformin inhibits the mitochondrial complex I in a manner similar to metformin (51). The biguanide-induced lactic acidosis results from insulin deficiency which leads to protein as well as fat catabolism and therefore accumulation of pyruvate. Because biguanides such as phenformin and metformin inhibit the pyruvate carboxylase, pyruvate cannot be metabolized in gluconeogenesis. In addition, pyruvate cannot be catabolized through the citric acid cycle because of the massive amount of acetyl-CoA derived from the fatty acid oxidation. Thus, the increased pyruvate is metabolized to lactate (33). Due to its higher affinity for mitochondrial membranes and the side effect of severe lactic acidosis, it was hypothesized that phenformin could have a higher anti-cancerous effect than metformin (51, 52). Since Met cells have a higher dependency on pyruvate it seems logical that they are more sensitive to phenformin treatment, as we observed both *in vitro* and *in vivo*. As many shRNA-”hits” in the initial and secondary screen were against mitochondria ribosomal proteins (*Mrp*) and other mitochondria-essential genes and reduced proliferation and/or induced cell death, choosing phenformin as therapeutic option to target mitochondria with a more specific mode of action may be a more valid therapeutic option.

Phenformin was proposed previously as a specific treatment for Lkb1-deficient but not p53-deficient lung tumors (53). In our system, both primary tumor and metastasis-derived cells are p53-deficient and we did not observe an effect of phenformin on tumor cell growth *in vitro* or *in vivo*. Instead, we showed that phenformin specifically targets the mitochondria in metastatic cancer cells which reduces early metastatic ability. In recent years it has been discussed whether the most prominent mitochondrial alteration in cancer — the Warburg effect — is caused by mitochondria that have been damaged over the course of tumor development, or whether the Warburg effect and the functionally altered mitochondria are a mere consequence of a favorable adaptation in order to proliferate under hostile conditions. Likewise, it remains unclear whether the change in mitochondria functionality in Met cells

observed in our study are required for their metastatic ability or if they are a result of the collateral damage that occurs during the metastatic process. Nevertheless, our findings provide novel insight into the metastatic cell state, identifying underlying functional differences and potentially therapeutic intervention opportunities for lung adenocarcinoma.

Supplementary Material

Refer to Web version on PubMed Central for supplementary material.

ACKNOWLEDGEMENTS

We thank Rosanna Ma, Santiago Naranjo, Eva Hahn, and Dagmar Thyssen for technical assistance; The Stanford Shared FACS facility for technical support; Sean Dolan and Alexandra Orantes for administrative support; Sven-Thorsten Liffers for help with bioinformatic illustrations; Verena Jendrossek, Johann Matschke and Mihaela Keller for support with hypoxia experiments; Former and current members of the Winslow, Grüner, Schramm, and Siveke laboratories for helpful comments.

We particularly thank Dr. John Doench and Dr. David Root from the Broad Institute Genetic Perturbation Platform and the Functional Genomics Consortium for providing critical reagents and technical expertise.

The TEM experiment described was supported by ARRA Award Number 1S10RR026780-01 from the National Center for Research Resources (NCRR).

C-HC was funded by a Stanford Dean's Fellowship and an American Lung Association Fellowship. BMG was a Hope Funds for Cancer Research Fellow supported by the Hope Funds for Cancer Research (HFCR-15-06-07). This work was supported by an Emmy Noether Award from the German Research Foundation (DFG, GR4575/1-1 to BMG), DOD CDMRP Lung Cancer Research Program LC130773 (to MMW) and NIH-R01-CA175336 (to MMW). PD is recipient of PhD fellowship from Cusanuswerk e.V. SS was supported by a Stanford Graduate Fellowship and the HHMI International Student Research Scholarship. DY was supported by a Stanford Graduate Fellowship and by a TRDRP Dissertation Award (24DT-0001).

REFERENCES

1. Siegel RL, Miller KD, and Jemal A, Cancer statistics, 2020. CA Cancer J Clin, 2020. 70(1): p. 7–30. [PubMed: 31912902]
2. Soda M, Choi YL, Enomoto M, Takada S, Yamashita Y, Ishikawa S, et al., Identification of the transforming EML4-ALK fusion gene in non-small-cell lung cancer. Nature, 2007. 448(7153): p. 561–6. [PubMed: 17625570]
3. Ding L, Getz G, Wheeler DA, Mardis ER, McLellan MD, Cibulskis K, et al., Somatic mutations affect key pathways in lung adenocarcinoma. Nature, 2008. 455(7216): p. 1069–75. [PubMed: 18948947]
4. Paez JG, Janne PA, Lee JC, Tracy S, Greulich H, Gabriel S, et al., EGFR mutations in lung cancer: correlation with clinical response to gefitinib therapy. Science, 2004. 304(5676): p. 1497–500. [PubMed: 15118125]
5. Haber DA, Bell DW, Sordella R, Kwak EL, Godin-Heymann N, Sharma SV, et al., Molecular targeted therapy of lung cancer: EGFR mutations and response to EGFR inhibitors. Cold Spring Harbor symposia on quantitative biology, 2005. 70: p. 419–26. [PubMed: 16869779]
6. Lynch TJ, Bell DW, Sordella R, Gurubhagavatula S, Okimoto RA, Brannigan BW, et al., Activating mutations in the epidermal growth factor receptor underlying responsiveness of non-small-cell lung cancer to gefitinib. The New England journal of medicine, 2004. 350(21): p. 2129–39. [PubMed: 15118073]
7. Pao W, Miller V, Zakowski M, Doherty J, Politi K, Sarkaria I, et al., EGF receptor gene mutations are common in lung cancers from "never smokers" and are associated with sensitivity of tumors to gefitinib and erlotinib. Proceedings of the National Academy of Sciences of the United States of America, 2004. 101(36): p. 13306–11. [PubMed: 15329413]

8. Comprehensive molecular profiling of lung adenocarcinoma. Nature, 2014. 511(7511): p. 543–50. [PubMed: 25079552]

9. Wang T, Wei JJ, Sabatini DM, and Lander ES, Genetic screens in human cells using the CRISPR-Cas9 system. Science, 2014. 343(6166): p. 80–4. [PubMed: 24336569]

10. Cheung HW, Cowley GS, Weir BA, Boehm JS, Rusin S, Scott JA, et al., Systematic investigation of genetic vulnerabilities across cancer cell lines reveals lineage-specific dependencies in ovarian cancer. Proceedings of the National Academy of Sciences of the United States of America, 2011. 108(30): p. 12372–7. [PubMed: 21746896]

11. Luo B, Cheung HW, Subramanian A, Sharifnia T, Okamoto M, Yang X, et al., Highly parallel identification of essential genes in cancer cells. Proceedings of the National Academy of Sciences of the United States of America, 2008. 105(51): p. 20380–5. [PubMed: 19091943]

12. Jackson EL, Olive KP, Tuveson DA, Bronson R, Crowley D, Brown M, et al., The differential effects of mutant p53 alleles on advanced murine lung cancer. Cancer Res, 2005. 65(22): p. 10280–8. [PubMed: 16288016]

13. Jackson EL, Willis N, Mercer K, Bronson RT, Crowley D, Montoya R, et al., Analysis of lung tumor initiation and progression using conditional expression of oncogenic K-ras. Genes & development, 2001. 15(24): p. 3243–8. [PubMed: 11751630]

14. Winslow MM, Dayton TL, Verhaak RG, Kim-Kiselak C, Snyder EL, Feldser DM, et al., Suppression of lung adenocarcinoma progression by Nkx2–1. Nature, 2011. 473(7345): p. 101–4. [PubMed: 21471965]

15. Weir BA, Woo MS, Getz G, Perner S, Ding L, Beroukhim R, et al., Characterizing the cancer genome in lung adenocarcinoma. Nature, 2007. 450(7171): p. 893–8. [PubMed: 17982442]

16. Chuang CH, Greenside PG, Rogers ZN, Brady JJ, Yang D, Ma RK, et al., Molecular definition of a metastatic lung cancer state reveals a targetable CD109-Janus kinase-Stat axis. Nat Med, 2017.

17. Laughney AM, Hu J, Campbell NR, Bakhoum SF, Setty M, Lavallee VP, et al., Regenerative lineages and immune-mediated pruning in lung cancer metastasis. Nat Med, 2020. 26(2): p. 259–269. [PubMed: 32042191]

18. Li CM, Chen G, Dayton TL, Kim-Kiselak C, Hoersch S, Whittaker CA, et al., Differential Tks5 isoform expression contributes to metastatic invasion of lung adenocarcinoma. Genes Dev, 2013. 27(14): p. 1557–67. [PubMed: 23873940]

19. Brady JJ, Chuang CH, Greenside PG, Rogers ZN, Murray CW, Caswell DR, et al., An Arntl2-Driven Secretome Enables Lung Adenocarcinoma Metastatic Self-Sufficiency. Cancer Cell, 2016. 29(5): p. 697–710. [PubMed: 27150038]

20. DuPage M, Dooley AL, and Jacks T, Conditional mouse lung cancer models using adenoviral or lentiviral delivery of Cre recombinase. Nat Protoc, 2009. 4(7): p. 1064–72. [PubMed: 19561589]

21. Moffat J, Grueneberg DA, Yang X, Kim SY, Kloepfer AM, Hinkle G, et al., A lentiviral RNAi library for human and mouse genes applied to an arrayed viral high-content screen. Cell, 2006. 124(6): p. 1283–98. [PubMed: 16564017]

22. Cheung HW, Cowley GS, Weir BA, Boehm JS, Rusin S, Scott JA, et al., Systematic investigation of genetic vulnerabilities across cancer cell lines reveals lineage-specific dependencies in ovarian cancer. Proc Natl Acad Sci U S A, 2011. 108(30): p. 12372–7. [PubMed: 21746896]

23. Ketela T, Heisler LE, Brown KR, Ammar R, Kasimer D, Surendra A, et al., A comprehensive platform for highly multiplexed mammalian functional genetic screens. BMC Genomics, 2011. 12: p. 213. [PubMed: 21548937]

24. Luo B, Cheung HW, Subramanian A, Sharifnia T, Okamoto M, Yang X, et al., Highly parallel identification of essential genes in cancer cells. Proc Natl Acad Sci U S A, 2008. 105(51): p. 20380–5. [PubMed: 19091943]

25. Dolan ME, Baldarelli RM, Bello SM, Ni L, McAndrews MS, Bult CJ, et al., Orthology for comparative genomics in the mouse genome database. Mamm Genome, 2015. 26(7–8): p. 305–13. [PubMed: 26223881]

26. Subramanian A, Tamayo P, Mootha VK, Mukherjee S, Ebert BL, Gillette MA, et al., Gene set enrichment analysis: a knowledge-based approach for interpreting genome-wide expression profiles. Proc Natl Acad Sci U S A, 2005. 102(43): p. 15545–50. [PubMed: 16199517]

27. Houtkooper RH, Mouchiroud L, Ryu D, Moullan N, Katsyuba E, Knott G, et al., Mitonuclear protein imbalance as a conserved longevity mechanism. Nature, 2013. 497(7450): p. 451–457. [PubMed: 23698443]
28. Meyer RR and Simpson MV, DNA biosynthesis in mitochondria. Differential inhibition of mitochondrial and nuclear DNA polymerases by the mutagenic dyes ethidium bromide and acriflavin. Biochem Biophys Res Commun, 1969. 34(2): p. 238–44. [PubMed: 5796743]
29. Zylber E, Vesco C, and Penman S, Selective inhibition of the synthesis of mitochondria-associated RNA by ethidium bromide. J Mol Biol, 1969. 44(1): p. 195–204. [PubMed: 5811827]
30. Rice AC, Keeney PM, Algarzae NK, Ladd AC, Thomas RR, and Bennett JP Jr., Mitochondrial DNA copy numbers in pyramidal neurons are decreased and mitochondrial biogenesis transcriptome signaling is disrupted in Alzheimer's disease hippocampi. J Alzheimers Dis, 2014. 40(2): p. 319–30. [PubMed: 24448779]
31. Chopra I, Hawkey PM, and Hinton M, Tetracyclines, molecular and clinical aspects. J Antimicrob Chemother, 1992. 29(3): p. 245–77. [PubMed: 1592696]
32. Protasoni M, Kroon AM, and Taanman JW, Mitochondria as oncotarget: a comparison between the tetracycline analogs doxycycline and COL-3. Oncotarget, 2018. 9(73): p. 33818–33831. [PubMed: 30333912]
33. Kwong SC and Brubacher J, Phenformin and lactic acidosis: a case report and review. J Emerg Med, 1998. 16(6): p. 881–6. [PubMed: 9848705]
34. Bridges HR, Jones AJ, Pollak MN, and Hirst J, Effects of metformin and other biguanides on oxidative phosphorylation in mitochondria. Biochem J, 2014. 462(3): p. 475–87. [PubMed: 25017630]
35. Demine S, Renard P, and Arnould T, Mitochondrial Uncoupling: A Key Controller of Biological Processes in Physiology and Diseases. Cells, 2019. 8(8).
36. Fennell M, Xiang Q, Hwang A, Chen C, Huang CH, Chen CC, et al., Impact of RNA-guided technologies for target identification and deconvolution. J Biomol Screen, 2014. 19(10): p. 1327–37. [PubMed: 25163683]
37. Elia I, Doglioni G, and Fendt SM, Metabolic Hallmarks of Metastasis Formation. Trends Cell Biol, 2018. 28(8): p. 673–684. [PubMed: 29747903]
38. Vander Heiden MG and DeBerardinis RJ, Understanding the Intersections between Metabolism and Cancer Biology. Cell, 2017. 168(4): p. 657–669. [PubMed: 28187287]
39. Warburg O, On respiratory impairment in cancer cells. Science, 1956. 124(3215): p. 269–70. [PubMed: 13351639]
40. Nelson DA, Tan TT, Rabson AB, Anderson D, Degenhardt K, and White E, Hypoxia and defective apoptosis drive genomic instability and tumorigenesis. Genes Dev, 2004. 18(17): p. 2095–107. [PubMed: 15314031]
41. Estrella V, Chen T, Lloyd M, Wojtkowiak J, Cornnell HH, Ibrahim-Hashim A, et al., Acidity generated by the tumor microenvironment drives local invasion. Cancer research, 2013. 73(5): p. 1524–1535. [PubMed: 23288510]
42. Gatenby RA, Gawlinski ET, Gmitro AF, Kaylor B, and Gillies RJ, Acid-mediated tumor invasion: a multidisciplinary study. Cancer Res, 2006. 66(10): p. 5216–23. [PubMed: 16707446]
43. Altieri DC, Mitochondrial dynamics and metastasis. Cell Mol Life Sci, 2019. 76(5): p. 827–835. [PubMed: 30415375]
44. Anderson GR, Wardell SE, Cakir M, Yip C, Ahn YR, Ali M, et al., Dysregulation of mitochondrial dynamics proteins are a targetable feature of human tumors. Nat Commun, 2018. 9(1): p. 1677. [PubMed: 29700304]
45. Faubert B, Li KY, Cai L, Hensley CT, Kim J, Zacharias LG, et al., Lactate Metabolism in Human Lung Tumors. Cell, 2017. 171(2): p. 358–371.e9. [PubMed: 28985563]
46. Elia I, Rossi M, Stegen S, Broekaert D, Doglioni G, van Gorsel M, et al., Breast cancer cells rely on environmental pyruvate to shape the metastatic niche. Nature, 2019. 568(7750): p. 117–121. [PubMed: 30814728]
47. Tasdogan A, Faubert B, Ramesh V, Ubellacker JM, Shen B, Solmonson A, et al., Metabolic heterogeneity confers differences in melanoma metastatic potential. Nature, 2020. 577(7788): p. 115–120. [PubMed: 31853067]

48. Falzone L, Salomone S, and Libra M, Evolution of Cancer Pharmacological Treatments at the Turn of the Third Millennium. 2018. 9(1300).

49. Roth KG, Mambetsariev I, Kulkarni P, and Salgia R, The Mitochondrion as an Emerging Therapeutic Target in Cancer. Trends Mol Med, 2019.

50. Yu M, Nguyen ND, Huang Y, Lin D, Fujimoto TN, Molkentine JM, et al., Mitochondrial fusion exploits a therapeutic vulnerability of pancreatic cancer. JCI Insight, 2019. 5.

51. Garcia Rubino ME, Carrillo E, Ruiz Alcala G, Dominguez-Martin A, J AM, and Boulaiz H, Phenformin as an Anticancer Agent: Challenges and Prospects. Int J Mol Sci, 2019. 20(13).

52. Pernicova I and Korbonits M, Metformin--mode of action and clinical implications for diabetes and cancer. Nat Rev Endocrinol, 2014. 10(3): p. 143–56. [PubMed: 24393785]

53. Shackelford DB, Abt E, Gerken L, Vasquez DS, Seki A, Leblanc M, et al., LKB1 inactivation dictates therapeutic response of non-small cell lung cancer to the metabolism drug phenformin. Cancer Cell, 2013. 23(2): p. 143–58. [PubMed: 23352126]

STATEMENT OF SIGNIFICANCE

This study characterizes altered mitochondria functionality of the metastatic cell state in lung cancer and opens new avenues for metastasis-specific therapeutic targeting.

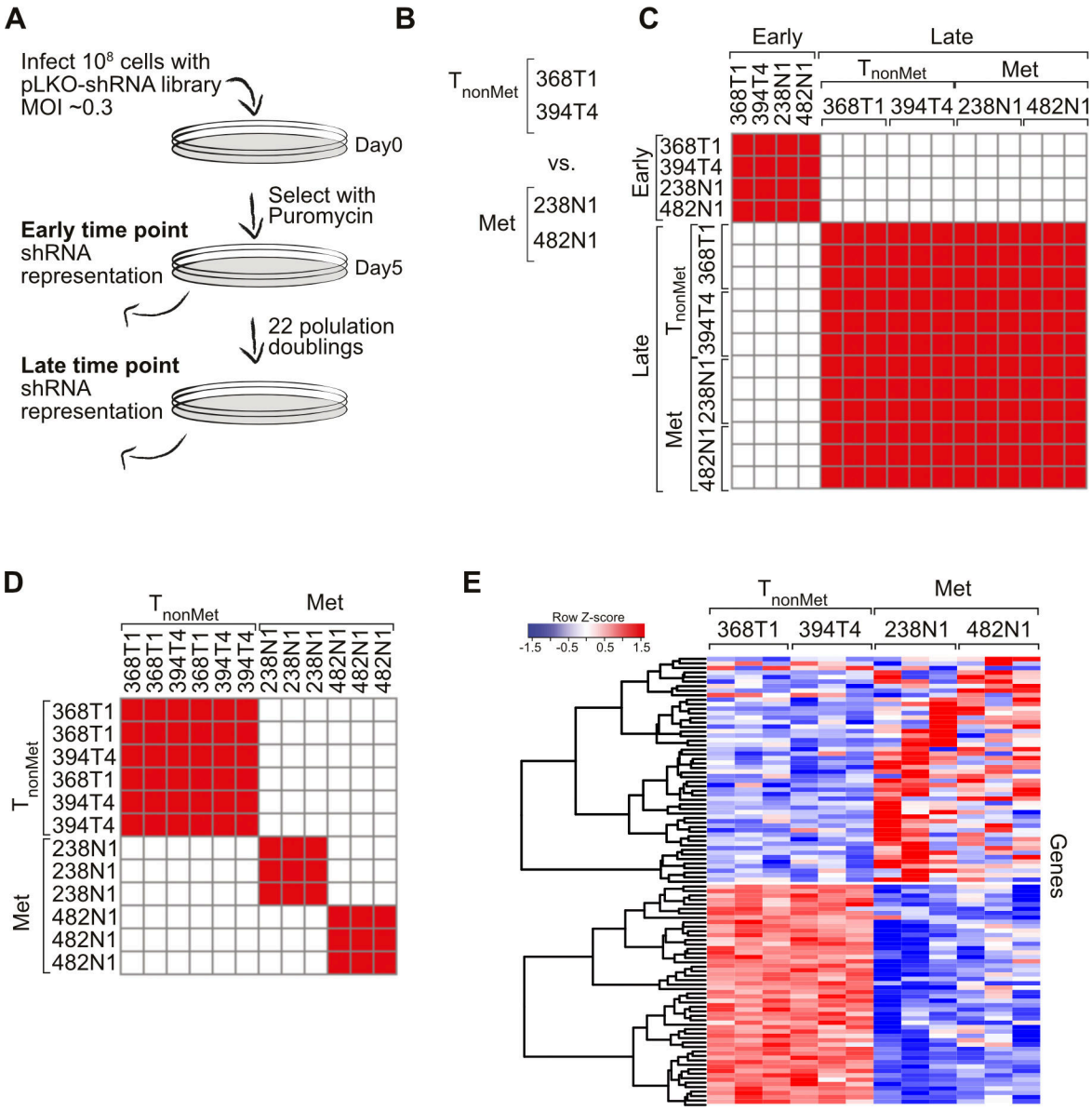

Figure 1. A genome-scale shRNA screen identifies candidate metastasis-specific lethal genes

A. Outline of the *in vitro* genome scale shRNA screen performed in two T_{nonMet} and two Met cell lines.

B. Cell lines derived from non-metastatic primary tumors (T_{nonMet}) and metastases (Met) used in this screen.

C. Clustering based on differential shRNA representation. Late time point samples have distinct global shRNA representation (driven by the loss of shRNAs that are lethal to all cells). Each box represents the measure of global correlation between the entire dataset for one cell line versus another.

D. Clustering based on differential shRNA representation. T_{nonMet} cell lines respond differently to shRNA treatment from Met cell lines, and Met cell lines are more divergent in their responses than T_{nonMet} lines. Each box represents the measure of global correlation between the entire dataset for one cell line versus another.

E. Top 50 genes that are specifically required for non-metastatic (top panel) and metastatic cancer cell viability (bottom panel). Heatmap shows the Weighted Sum metric of shRNA representation for each gene after knockdown

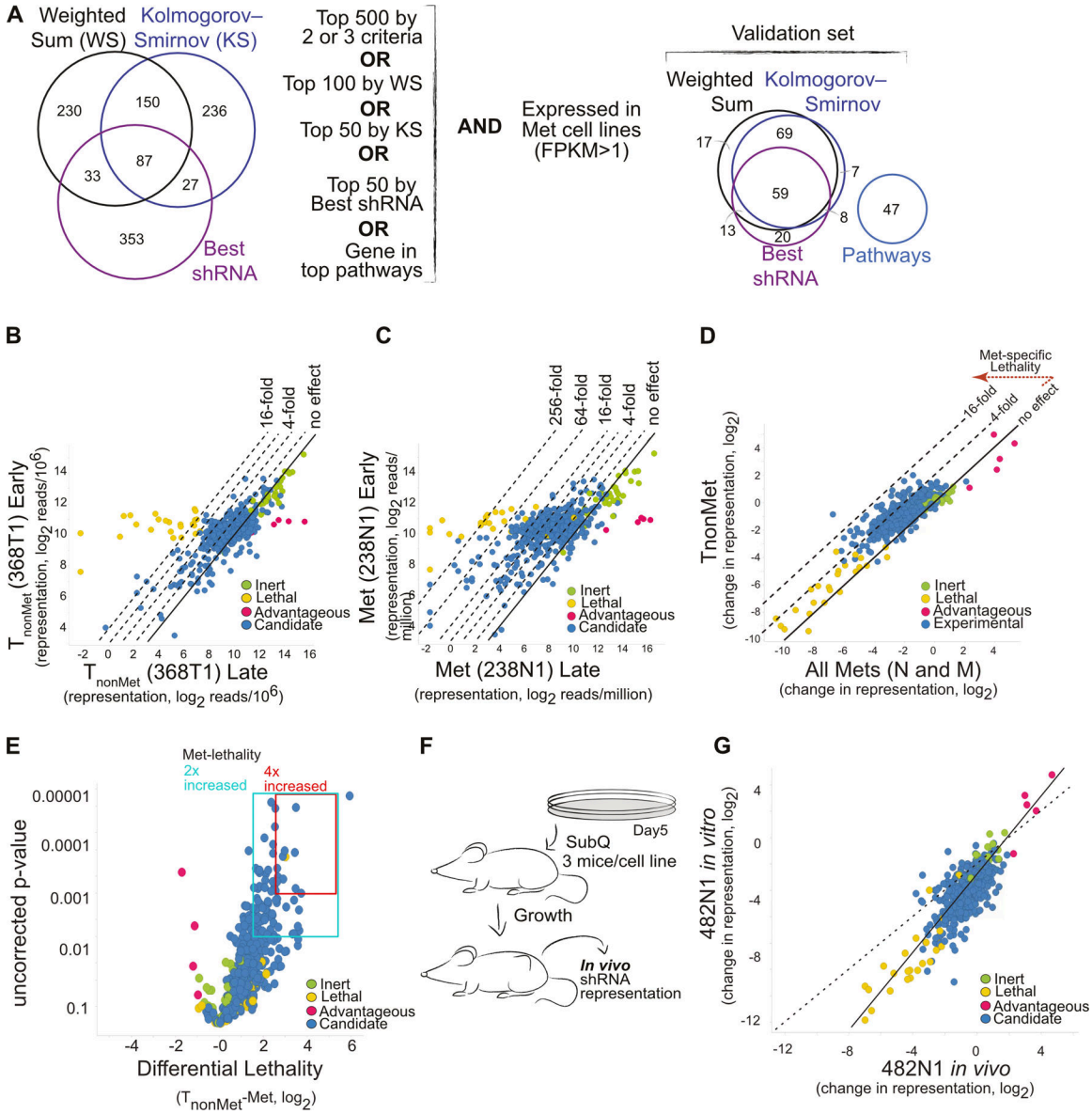

Figure 2. Validation of metastasis specific lethal/sick genes

A. Criteria for choosing genes for validation. Three methods were performed to uncover genes with a differential effect on Met cells lines and 240 candidate genes were chosen based on the depicted criteria.

B, C. Representation before (Early) and after (Late) 20 doubling *in vitro*. In both T_{nonMet} (**B**, 368T1) and Met (**C**, 238N1) cells the representation of lethal genes is reduced, inert genes are unchanged, and advantageous genes increase. Candidate genes have a great reduction in representation in the Met cells. Each dot represents one shRNA.

D. Differential effect of each shRNA on Met versus T_{nonMet} cells. The difference in the change in representation between the Early and Late timepoint for each cell line is indicated as Met-specific effect with many genes having a > 4x greater effect in the Met cells. Each dot represents one shRNA.

E. Differential effect on Met cells plotted against an un-normalized p-value uncovers top candidate genes with the greatest fold effect and high reproducibility. Each dot represents one shRNA. The boxes indicate candidate shRNAs that are at least two-fold (blue box) or at least four-fold (red box) increased in Met cells, meaning they are at least two-fold or four-fold more lethal for Met than for T_{nonMet} cells.

F. Outline of a parallel *in vivo* screen to assess the impact of candidate genes on cancer cell growth *in vivo*.

G. General agreement of *in vitro* and *in vivo* effects on Met cells (482N1).

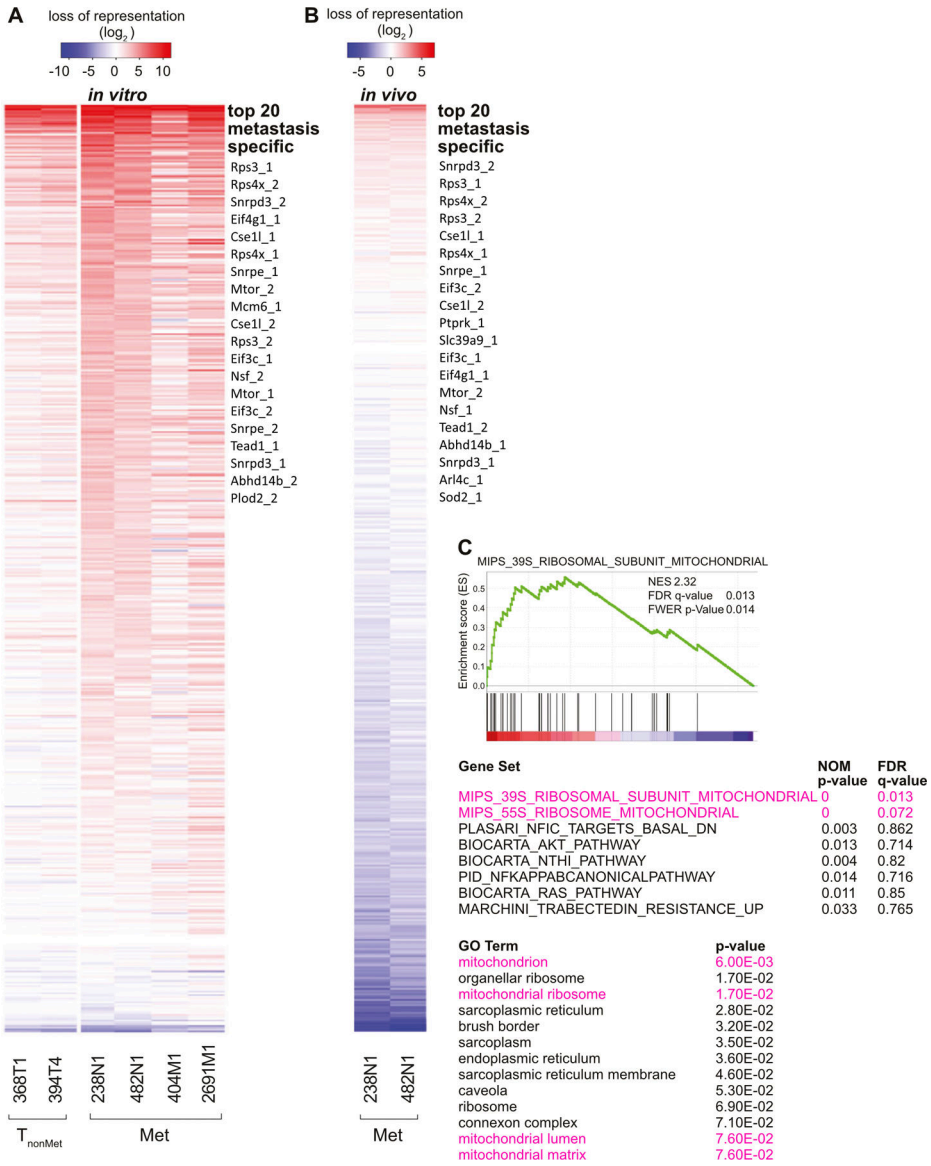

Gene Set	NOM p-value	FDR q-value
MIPS_39S_RIBOSOMAL_SUBUNIT_MITOCHONDRIAL	0	0.013
MIPS_55S_RIBOSOME_MITOCHONDRIAL	0	0.072
PLASARI_NFIC_TARGETS_BASAL_DN	0.003	0.862
BIOCARTA_AKT_PATHWAY	0.013	0.714
BIOCARTA_NTHI_PATHWAY	0.004	0.82
PID_NFKAPPABCANONICALPATHWAY	0.014	0.716
BIOCARTA_RAS_PATHWAY	0.011	0.85
MARCHINI_TRABECTEDIN_RESISTANCE_UP	0.033	0.765

GO Term	p-value
mitochondrion	6.00E-03
organellar ribosome	1.70E-02
mitochondrial ribosome	1.70E-02
sarcoplasmic reticulum	2.80E-02
brush border	3.20E-02
sarcoplasm	3.50E-02
endoplasmic reticulum	3.60E-02
sarcoplasmic reticulum membrane	4.60E-02
caveola	5.30E-02
ribosome	6.90E-02
connexon complex	7.10E-02
mitochondrial lumen	7.60E-02
mitochondrial matrix	7.60E-02

Figure 3. Metastasis specific effect of mitochondria-targeting strategies.

A. Heatmap of the changes of shRNA representation in the secondary *in vitro* screen, ranked by their highest effect on Met cells (red). The corresponding data tables with gene/shRNA names and data values can be found in Data Table 9. The top 20 shRNAs that had the highest metastasis-specific effect *in vitro* are listed next to the heatmap. The numbers behind the gene name indicate which of the two shRNAs against that gene were identified, as two shRNAs per gene were used in the second screen.

B. Heatmap of the changes of shRNA representation in the secondary *in vivo* screen, ranked by their highest effect on Met cells (red). The corresponding data tables with gene/shRNA names and data values can be found in Data Table 9. The top 20 shRNAs that had the highest metastasis-specific effect *in vivo* are listed next to the heatmap. The numbers behind the gene name indicate which of the two shRNAs against that gene were identified, as two shRNAs per gene were used in the second screen.

C. Gene set enrichment analysis (GSEA) of genes that lose representation specifically in Met cell line samples during *in vitro* culture. The top panel illustrated an example of the most Met-specific lethal pathway. Vertical bars are genes represented in the gene set/pathway sorted by essentiality (left: more essential) and the enrichment score is graphed above (green trace). The middle panel lists the pathways that elicit the most Met-specific lethal shRNA treatment response determined by GSEA analysis, the only significant top gene sets ($p < 0.05$, FDR < 0.25) represent the mitochondria ribosome and are highlighted in pink. The bottom panel lists the results of the Gene Ontology (GO) Term analysis. It identifies the mitochondrion and the mitochondrial ribosome as top cellular complexes to target for metastasis-specific lethality.

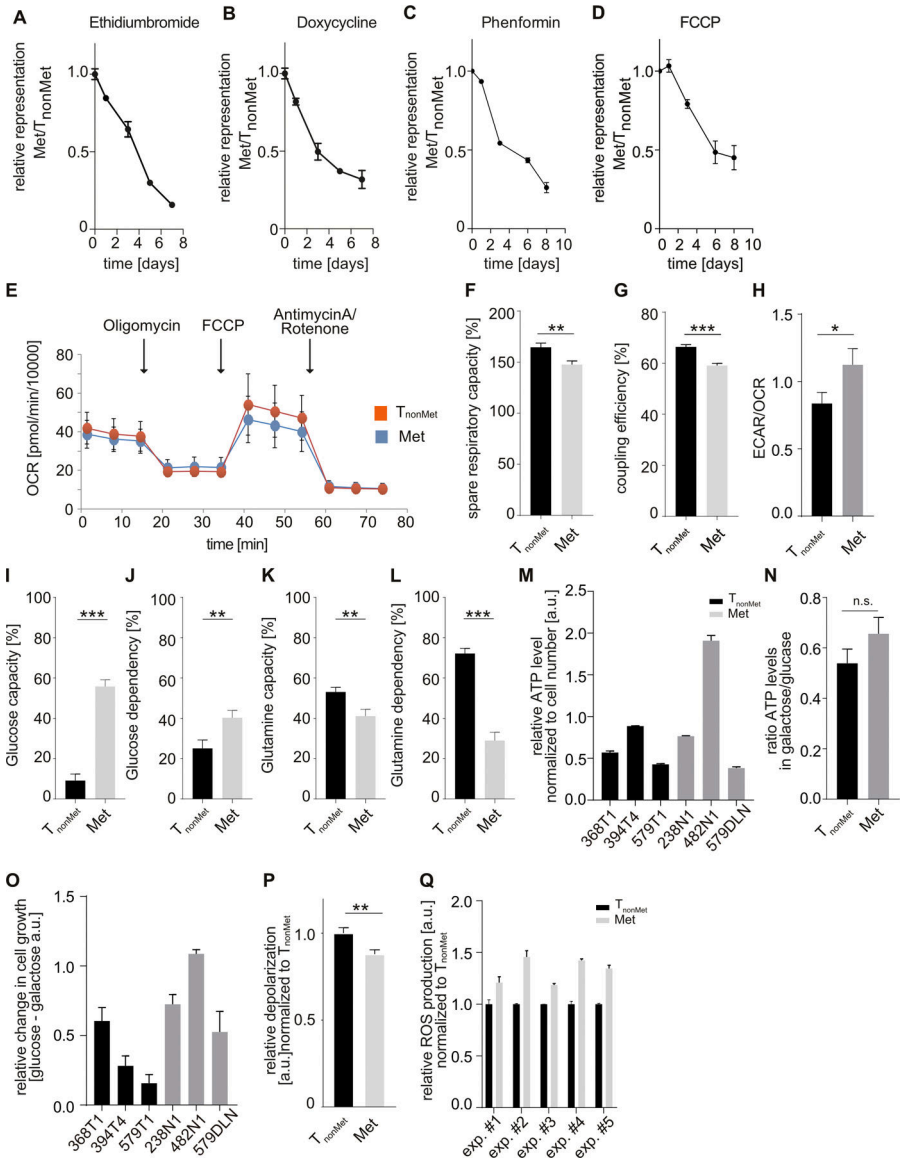

Figure 4. Metastasis cell lines are more susceptible to mitochondria targeting therapy due to altered mitochondria functionality.

A-D. *In vitro* competition assay of Met (482N1) and T_{nonMet} (394T4) cell lines treated with 50ng/ml ethidium bromide (**A**), 15 μg/ml doxycycline (**B**), 200 μM phenformin (**C**), or 2 μM FCCP (**D**) shows higher treatment effect on Met cells. Data normalized to untreated control; one representative experiment of at least three independent experiments tested in triplicate is shown. Error bars indicate S.D.; if the error bar is missing, the symbol was larger than the error bar.

E-H. Seahorse analysis of Met and T_{nonMet} cell lines (n = 3 each) to measure oxygen consumption rate. Cells were treated with compounds as indicated in (**E**), according to assay instructions. Met cell lines show lower spare respiratory capacity (**F,** $p = 0.0039$) and reduced coupling efficiency (**G,** $p < 0.0001$). Analysis of ECAR/OCR ratio illustrates the higher use of gylcolysis in Met cells (**H**). Three independent experiments measured in quadruplicate, one representative experiment is shown. Error bars indicate SEM.

I-L. Seahorse MitoFuelFlexTest analysis of Met and T_{nonMet} cell lines (n = 3 each) to measure fuel capacity and dependency. Met cells show a higher dependency on glycolysis-derived pyruvate (**I**, $p < 0.001$; and **J**, $p = 0.0094$) and they are less able to use glutamine, indicating reduced rate of glutamine as fuel during oxidative phosphorylation (**K,** $p = 0.0057$; and **L**, $p < 0.0001$). Error bars indicate SEM.

M. Analysis of ATP levels by reversed cell titer glow assay normalized to cell number in Met and T_{nonMet} cell lines cultured in galactose containg media (n = 3 each). Three independent experiments measured in triplicate, one representative experiment is shown. Error bars indicate SEM.

N. Analysis of relative by reversed cell titer glow assay normalized to cell number in Met and T_{nonMet} cell lines cultured in galactose containg media and glucose-containing media (n = 3 each, $p = 0.1377$). Data is calculated as ratio galactose/glucose. Error bars indicate SEM.

O. Analysis of relative cell growth in glucose-containing media and galactose-containing media. Data is calculated as delta [glucose-galactose]. Three independent experiments measured in triplicate, one representative experiment is shown. Error bars indicate SEM.

P. JC1 staining of Met (n=2) and T_{nonMet} (n=2) cell lines to measure relative depolarization by flow cytometry. Error bars indicate SEM; $p = 0.0032$

Q. Reactive oxygen species (ROS) staining of T_{nonMet} (**H**) and Met (**I**) cell lines to measure relative ROS production by flow cytometry. Five independent experiments (exp. #1 through 5) were performed, each with 2 T_{nonMet} and 2 Met cell lines. Shown are the means of each independent experiment normalized to the mean of T_{nonMet} cells per respective experiment. Error bars indicate SD.

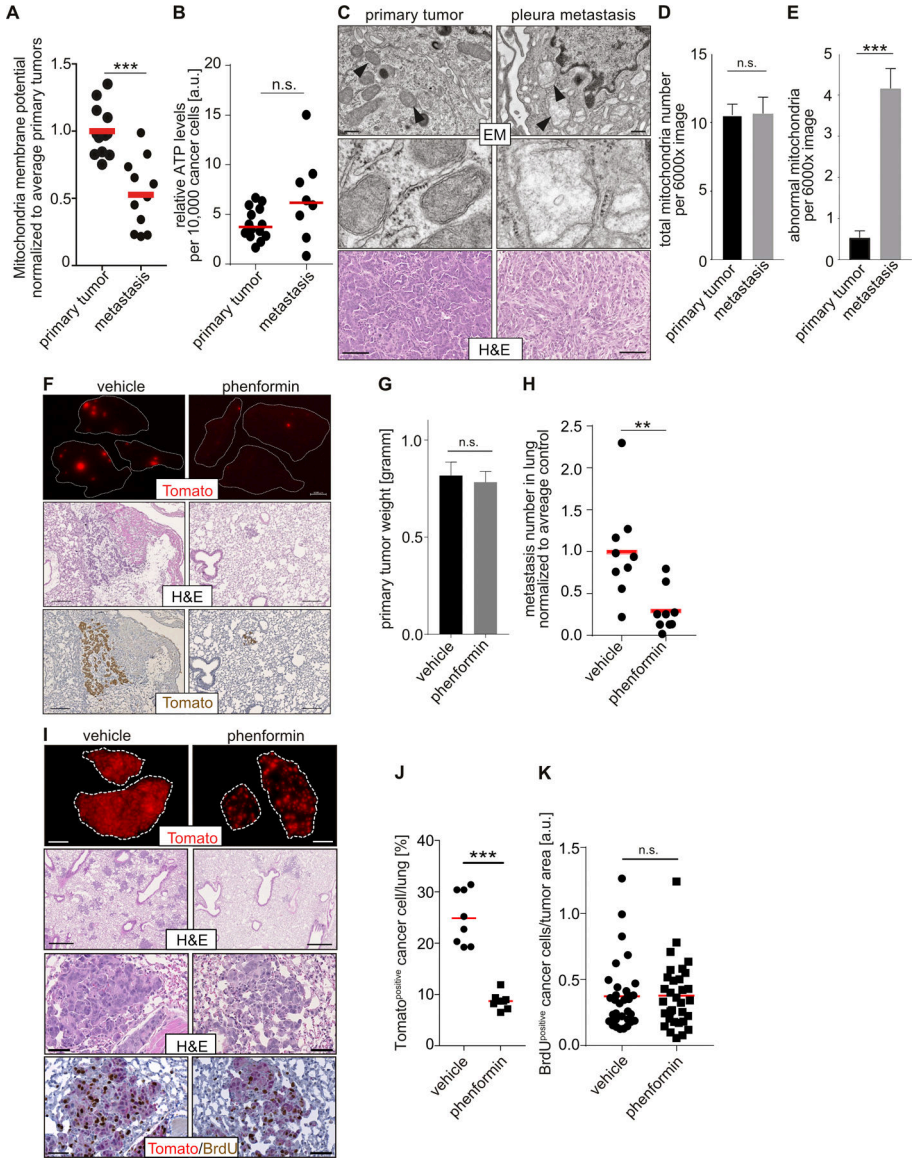

Figure 5. Mitochondria of metastasis in *in vivo* mouse models of lung cancer have reduced functionality and are a target for anti-metastatic treatment.

A. Mitotracker deep red analysis by flow cytometry of Lineage^{negative};DAPI^{positive} cells sorted from primary tumors and metastasis in *Kras^{G12D};Trp53^{KO};R26^{Tomato}* lung cancer mice (n = 5 mice) shows significantly reduced membrane potential in metastasis cells compared to primary tumor cells ($p < 0.001$). Cell number staining artifacts were controlled for by spiked in GFP^{+} cells as staining control. Each dot represents one primary tumor or one metastasis sample, the red line indicates the mean.

B. Analysis of ATP levels by reversed cell titer glow assay of Lineage^{negative};DAPI^{positive} cells sorted from primary tumors and metastasis in *Kras^{G12D};Trp53^{KO}* lung cancer mice (n = 3 mice) shows no significant difference in ATP levels between primary tumor and metastasis cells. Each dot represents one primary tumor or metastasis sample.

C-E. Electron microscopy analysis of tissue sections from primary tumors and pleura metastasis in *Kras^{G12D};Trp53^{KO}* lung cancer mice (n = 2). Mitochondria in metastasis tissue

samples show destroyed morphology with less density and bridging (**C**, upper panels 2000x resolution, middle panels 6000x resolution, lower panels show corresponding H&E staining, error bars = 400nm upper panel, error bars = 100 μm lower panel). Quantification of total number of mitochondria in EM sections (**D**) shows no significant ($p = 0.5455$) difference between sections from primary tumors and metastasis, but a significantly higher ($p < 0.0001$) number of abnormal mitochondria in metastatic tissue sections (**E**). Error bars indicate SEM. At least 15 pictures per sample were analyzed.

F-H. Mice were subcutaneously injected with a metastatic lung cancer cell line and treated with either phenformin (100 mg/kg p.o., n = 9 mice) or vehicle control (n = 9 mice) daily starting 7 days after injection. 21 days after injection, lungs were harvested and analyzed by fluorescent stereomicroscope (**F,** upper panel, scale bar = 1 mm), H&E staining (**F**, middle panel, scale bar = 100 μm), and IHC for Tomato (**F**, lower panel, scale bar = 100 μm). While primary tumor weight was not significantly different between treated and control animals (**G**, $p = 0.86$), the number of metastasis in the lungs was significantly reduced upon phenformin treatment (**H**, $p = 0.0025$). Each dot represents one sample, the red line indicates the mean.

I-K. 579DLN Met cells were pretreated *in vitro* with phenformin (200 μM) or vehicle control for 48 hours and then intravenously injected into recipient mice. Mice were then treated with either phenformin (100 mg/kg p.o., n = 8 mice) or vehicle control (n = 8 mice) daily starting at the day of injection. 8 days after injection, lungs were harvested and analyzed by fluorescent stereomicroscope (**I,** upper panel, scale bar = 1 mm), H&E staining (**I**, second, panel, scale bar = 500 μm, third panel, scale bar = 50 μm), and IHC for Tomato and BrdU (**I**, lower panel, scale bar = 50 μm) and flow cytometry (**J**). The percentage of $Tomato^{positive}$ cancer cells in the lungs was significantly reduced upon pretreatment with phenformin ($p = 0.0002$). Each dot represents one sample, the red line indicates the mean. (**K**) Quantification of BrdU positive cancer cells normalized to tumor area, $p = 0.7338$ = n.s.; each dot represents one analyzed random IHC image, 4 images per mouse were analyzed; the red lines indicate the mean.